Supporting Information

Strain-induced charge delocalization achieves ultralow exciton binding energy toward efficient photocatalysis

Junyuan Duan,‡[ab] Yinghe Zhao,‡[a] Yu Wu,[a] Youwen Liu,*[a] Junnian Chen,[e] Ruoou Yang,[a] Jiazhao Huang,[a] Chuanqi Luo,[a] Mao Wu,[a] Xiaodong Zheng,[d] Pengyu Li,[a] Xueliang Jiang,*[b] Jianguo Guan*[c] and Tianyou Zhai[a]

[a]State Key Laboratory of Materials Processing and Die & Mould Technology, and School of Materials Science and Engineering, Huazhong University of Science and Technology, Wuhan 430074, China;

[b]Hubei Key Laboratory of Plasma Chemistry and New Materials, School of Materials Science and Engineering, Key Laboratory of Green Chemical Engineering Process of Ministry of Education, Engineering Research Center of Phosphorus Resources Development and Utilization of Ministry of Education, Wuhan Institute of Technology, Wuhan 430205, China;

[c]State Key Laboratory of Advanced Technology for Materials Synthesis and Processing, Wuhan University of Technology, Wuhan 430070, China;

[d]Department of Applied Physics, The Hong Kong Polytechnic University, Kowloon, Hong Kong, China;

[e]School of Materials Science & Engineering, Hubei University, Wuhan 430062, China

* **Corresponding authors.** E-mail: ywliu@hust.edu.cn, guanjg@whut.edu.cn, jiangxl@wit.edu.cn

‡ These authors contributed equally to this work.

Experimental

Samples synthesis

s-Ta_2O_5 NRs were prepared by a hydrothermal route. A mixture of 52 mL of water, 100 mg of tantalum powders, 325 μL of hydrofluoric acid, and 15 mL of a 30 wt% hydrogen peroxide solution was prepared and transferred into a 100 mL Teflon-lined autoclave. This autoclave was subsequently heated to 240 °C for 12 hours inside an oven. Upon cooling down to room temperature naturally, the resulting white precipitate was isolated by centrifugation, thoroughly rinsed with ethanol and water, and then dried at 60°C for 6 hours, yielding a dry white powder. Ta_2O_5 NRs were produced by annealing the s-Ta_2O_5 nanorod samples at 750 °C for 4 hours in a tubular furnace, under atmospheric air, and allowing them to cool naturally.

Characterizations

The samples were characterized using X-ray diffractometer (XRD, Cu Kα, λ = 1.5405 Å, D2 PHASER, Bruker), a confocal Raman system (Alpha 300RS+, WITec), scanning electron microscopy (SEM, Hitachi S-4800), and high-resolution transmission electron microscopy (HRTEM, FEI Tecnai G2 F30) with an X-ray energy dispersive spectrometer (EDS), a spherical aberration-corrected high-resolution transmission electron microscope (Thermofisher Themis Z, FEI), atomic force microscopy (AFM, Dimension Icon, Bruker), electron spin resonance spectrometer (Bruker EMXplus A300), X-ray photoelectron spectroscopy (XPS, AXIS-ULTRA DLD-600W), UV-Vis spectrophotometer (UV-3600i Plus, Shimadzu), X-ray absorption fine structure spectra (XAFS) were collected at the BL11B beamline of the Shanghai Synchrotron Radiation Facility (SSRF). Electrochemical impedance spectra (EIS) were recorded in a 1M Na_2SO_4 solution at -1.7 V (vs. Ag/AgCl) over a frequency range of 0.1 to 10^6 Hz, with a 10 mV amplitude, on an electrochemical workstation (CHI760E, Chenhua). The samples were mounted on an Au substrate for surface potential measurements using AFM with a Kelvin probe. Temperature-dependent photoluminescence (PL) spectra and time-resolved transient PL decay were assessed using an Edinburgh FLS 980 spectrofluorometer with excitation wavelength of 325 nm.

Photocatalytic performance test

Photocatalytic hydrogen production tests are performed in a sealed quartz vessel with a capacity of roughly 150 mL and a diameter of about 6.3 cm. To begin, 80 mg of the catalyst is ultrasonically dispersed in 100 mL of an aqueous methanol solution with a 20% volume fraction. After achieving a uniform dispersion, the mixture is transferred to the reactor. The system utilizes a top-illumination method, with a 300 W high-pressure mercury lamp serving as the light source. The gas products are subsequently analyzed using an online-connected gas chromatograph.

DFT calculations

DFT calculations were conducted using the Vienna Ab initio Simulation Package (VASP) within the framework of density functional theory (DFT),[1] complemented by post-processing via VASPKIT.[2] The Perdew-Burke-Ernzerhof (PBE) generalized gradient approximation (GGA) was employed for the exchange-correlation potential.[3] The energy cutoff was established at 520 eV. Ion relaxation and electron self-consistency were set to 0.02 eV/Å and 1×10^{-6} eV, respectively. To accurately account for van der Waals forces, the DFT-D3 method with long-range dispersion corrections was applied. Ta_2O_5 model included 77 atoms, and the K-point grid was chosen to be 5×1×1.

To investigate the bonding characteristics in Ta_2O_5 with ~3% tensile strain along [001], the electron localization function (ELF) was calculated according to the formula:[4]

$$ELF(r)= \{1 + [K(r)/Kh[\rho(r)]]^2\}^{-1} \quad (1)$$

K(r) represents the curvature of the electron pair density for electrons with identical spin states, ρ(r) is the electron density at position r, and Kh[ρ(r)] is the curvature of a homogeneous electron gas with the same electron density ρ.

DFT calculations for the hydrogen evolution reaction (HER) were performed using identical settings and parameters as those for the structural optimization. Atomic positions were refined until the forces on each atom fell below 0.002 eV/Å. Ta_2O_5 (001) with a 15 Å vacuum layer was utilized. The HER reaction process is depicted as follows:

$$H^* + e^- \rightarrow 1/2\ H_2 \quad (2)$$

The reaction Gibbs free energy (ΔG) is given by:

$$\Delta G = \Delta E + \Delta E_{ZPE} - T\Delta S \quad (3)$$

In this equation, ΔE is the adsorption energy, and T is the temperature, ΔE_{ZPE} and ΔS are the changes in zero-point energy and entropy, respectively. Considering the negligible vibrational entropy of adsorbed H*, the adsorption entropy for $1/2H_2$, denoted ΔSH, is estimated as $1/2S^0H_2$, where S^0H_2 is the entropy of gaseous H_2 under standard conditions.[5]

E_b is described by the Wannier-Mott exciton model, which uses the formula:[6]

$$E_b=\mu E_0/m_0\varepsilon_r^2 \quad (4)$$

Here, the reduced exciton mass is given by: $1/\mu=1/m_e+1/m_h$. The Rydberg energy (E_0) is 13.6 eV. The dielectric constant ε_r is calculated using density-functional perturbation theory (DFPT), as implemented in VASP. This process involves computing the permittivity tensor for the bulk unit cell and the Born effective charge tensor, which helps determine the ionic contribution to the dielectric function.[7] The K-point lattice is discretized using an inverse spatial resolution of $2\pi \times 0.04$ Å^{-1}, which establishes the density of scattering points. The effective masses of electrons and holes are ascertained through an energy band fitting method, utilizing a program integrated within VASPKIT.

Supporting Figures

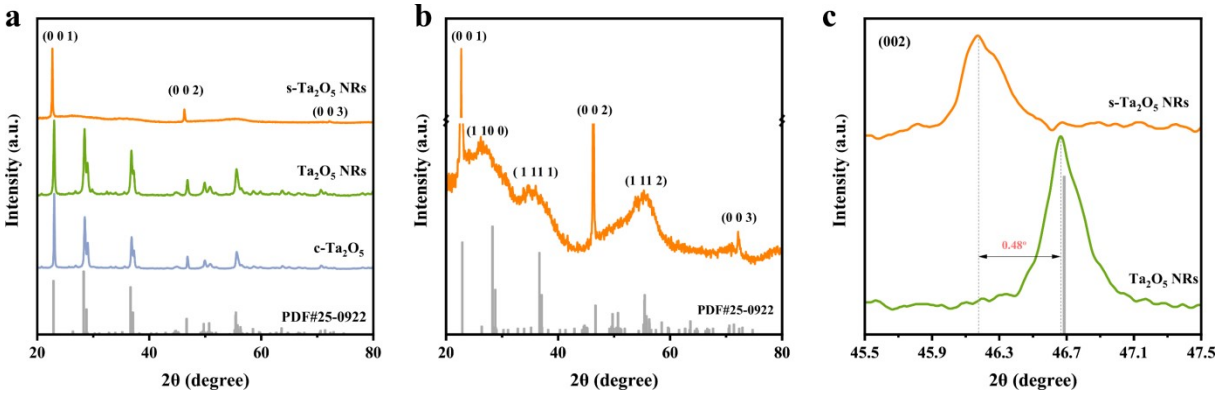

Fig. S1 XRD patterns of typical s-Ta_2O_5 NRs. (a) Comparisons of s-Ta_2O_5, Ta_2O_5 NRs, and c-Ta_2O_5 with standard PDF 250922. (b) Enlarged intensity of the XRD pattern. (c) Enlarged view of the (002) peak in the XRD patterns for both s-Ta_2O_5 NRs and Ta_2O_5 NRs. The XRD pattern of the s-Ta_2O_5 NRs displays distinct diffraction peaks at 2θ angles of approximately 22.71°, 46.28°, and 72.14°, corresponding to the (0 0 1), (0 0 2), and (0 0 3) planes of the orthorhombic Ta_2O_5 phase (PDF# 25–0922), indicating a preferential orientation along the c-axis. Closer examination reveals additional, though less pronounced, peaks at 2θ values of 26.2°, 36.2°, and 55.3°, associated with the (1 10 0), (1 11 1), and (1 12 1) planes, respectively (Fig. S1b). The broadness and reduced intensity of these peaks suggest lower crystallinity or a partially amorphous nature in these orientations. After annealing at 750 °C, Ta_2O_5 NRs (Fig. S6) exhibited the diffraction peaks of c-Ta_2O_5 (Fig. S7) in both position and intensity. Analyzing the XRD patterns for s-Ta_2O_5 and Ta_2O_5 NRs shows minor peak shifts in the (0 0 1) and (0 0 2) planes of the s-Ta_2O_5 NRs sample towards lower angles (Fig. 1c and Fig. S1c), with displacements of 0.24° and 0.48°, respectively. These shifts suggest an expansion in lattice spacing and the introduction of a slight tensile strain within the crystal lattice along the [001] (c-axis).

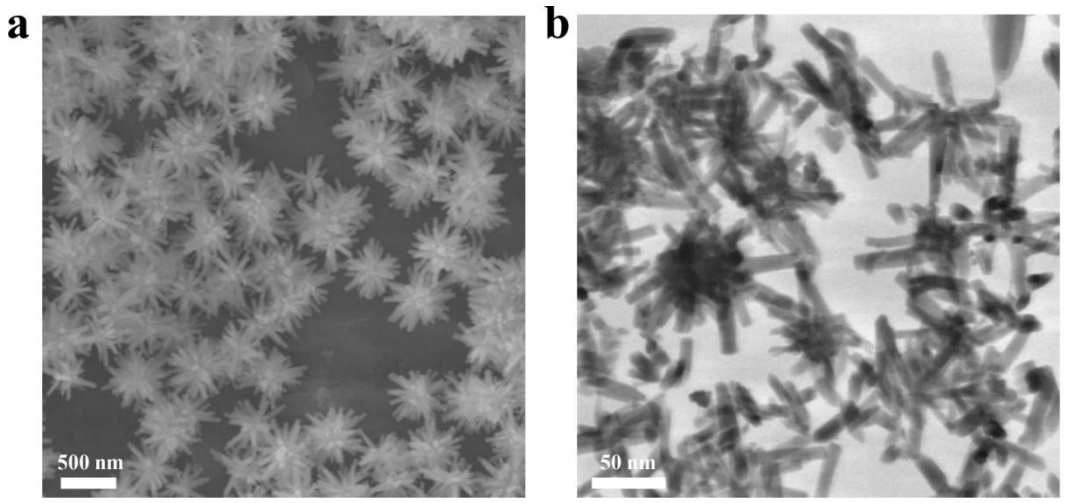

Fig. S2 Morphology characterization of s-Ta_2O_5 NRs. (a) SEM and (b) TEM image Fig. S2 demonstrate that the typical s-Ta_2O_5 NRs exhibits nanorods shapes with diameters ranging from 20 to 50 nm and lengths extending from 100 to 300 nm.

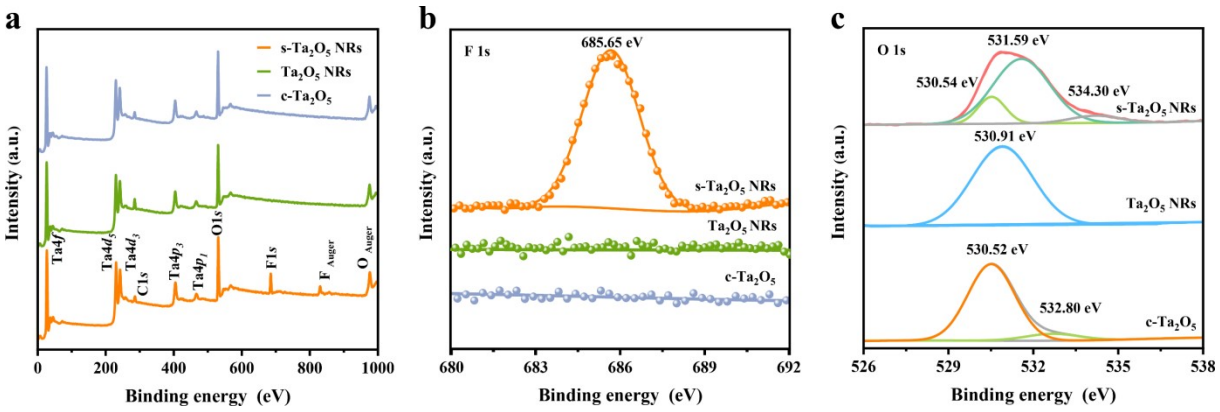

Fig. S3 XPS spectra of various Ta_2O_5 samples. (a) Full spectra, (b) F 1*s* orbital spectra. (c) O 2*p* orbital spectra.

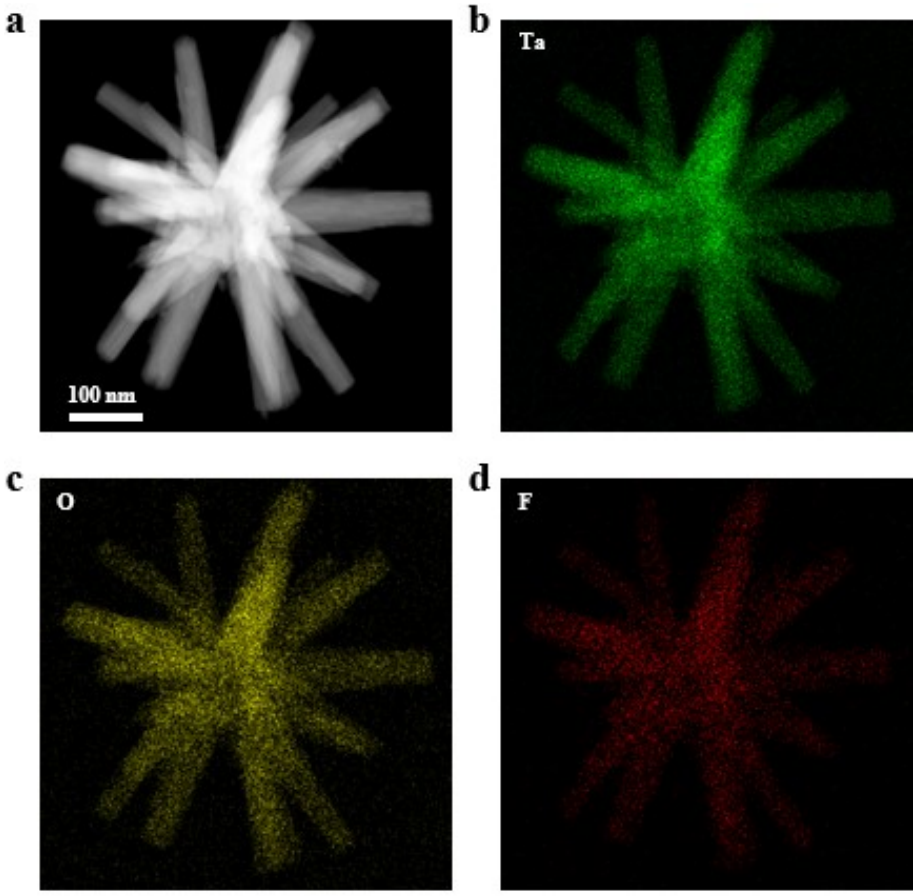

Fig. S4 EDS mapping of s-Ta_2O_5 NRs. EDS mapping was utilized to elucidate the distribution of F element within s-Ta_2O_5 NRs and its consequent effect on the nanorod's structure. Fig. S4 illustrates a homogeneous dispersal of Ta, O, and F elements throughout the nanorods, with a notably weaker signal for F, suggesting its minor presence.

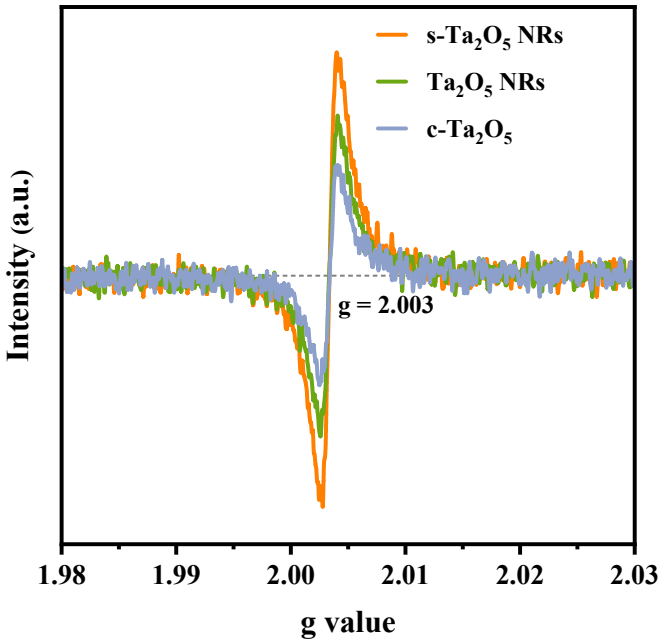

Fig. S5 ESR spectra of s-Ta_2O_5 NRs, Ta_2O_5 NRs and c-Ta_2O_5. The ESR signal at g=2.003, indicative of surface oxygen defects, is clearly observed. Notably, the signal is most pronounced in s-Ta_2O_5 NRs, implying a higher concentration of oxygen defects.

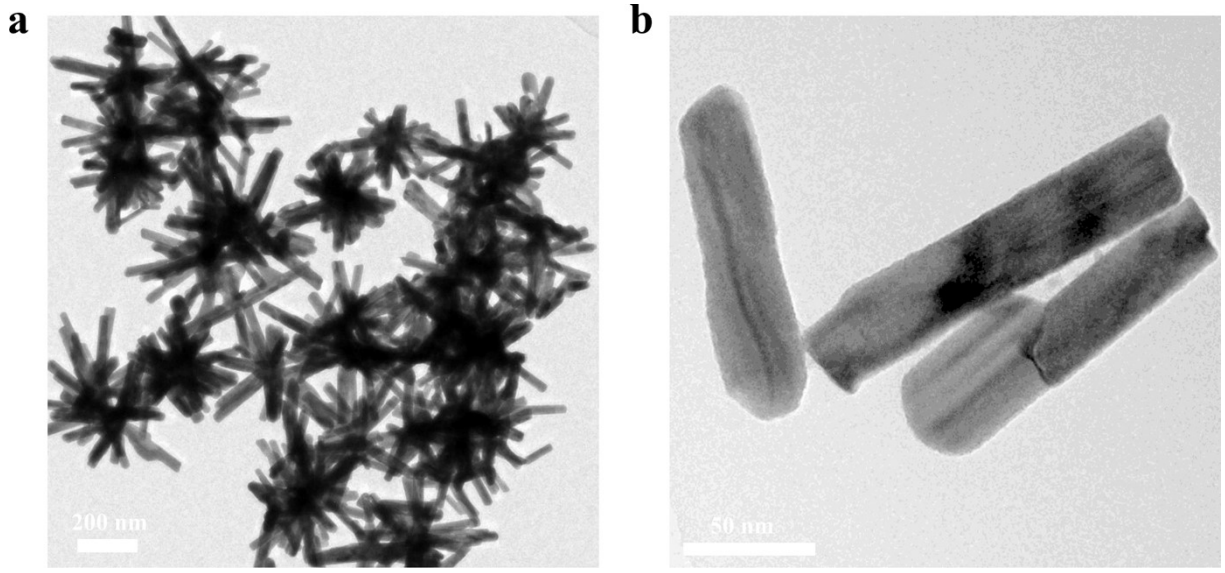

Fig. S6 TEM images of Ta_2O_5 NRs. Fig. S6 shows that the Ta_2O_5 NRs display sizes and shapes comparable to those of s-Ta_2O_5 NRs (Fig. S2).

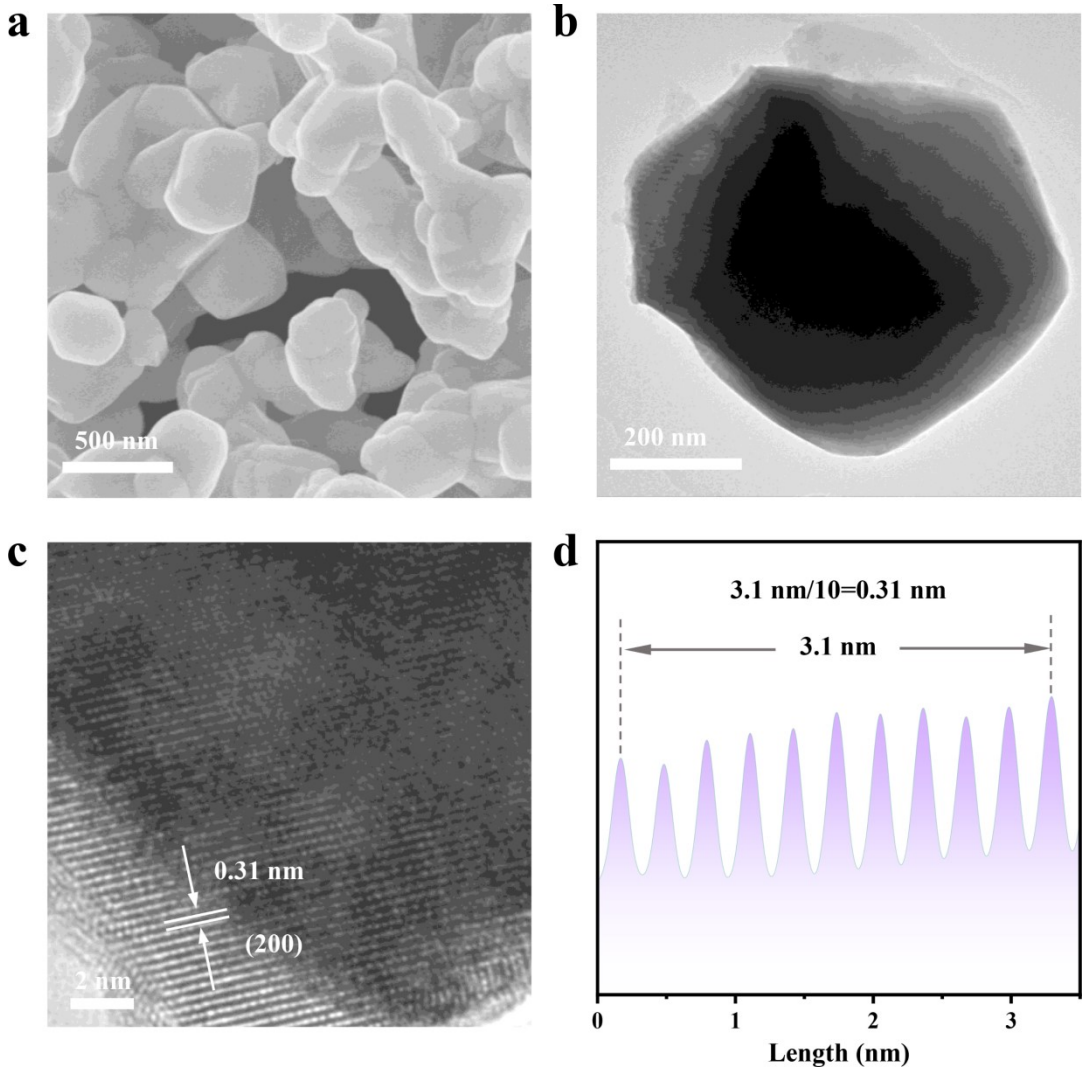

Fig. S7 Structural characterizations of c-Ta_2O_5 samples. (a) SEM image. (b) TEM image. (c) HRTEM image. (d) Lattice fringe interplanar spacings. Fig. S7a, b illustrate that c-Ta_2O_5 particles vary in size from 400 nm to 1μm. The HRTEM image of c-Ta_2O_5 shows an interplanar spacing of 0.31 nm for the (200) plane, aligning with the characteristic orthorhombic Ta_2O_5 crystal structure.

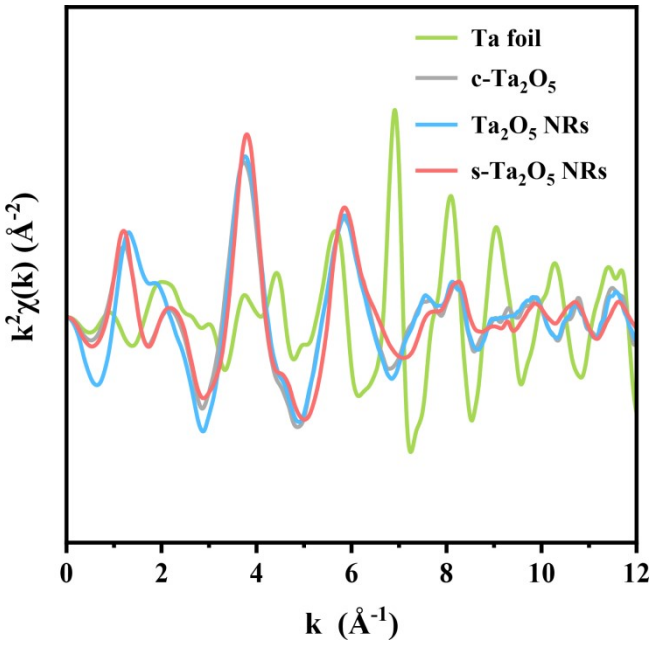

Fig. S8 $k^2\chi(k)$ oscillation curves. Fig. S8 distinguishes the low-frequency oscillations characteristic of the lighter oxygen atoms from the high-frequency oscillations associated with the heavier Ta atoms.

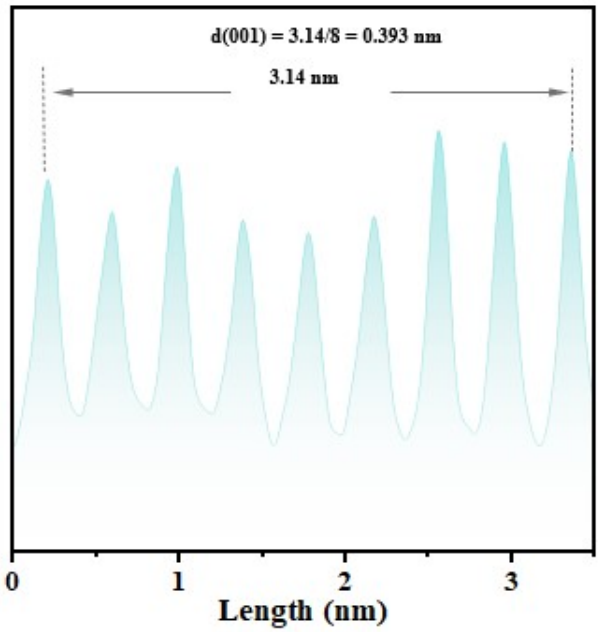

Fig. S9 Lattice fringe interplanar spacings marked by the red line in Fig. 2a.

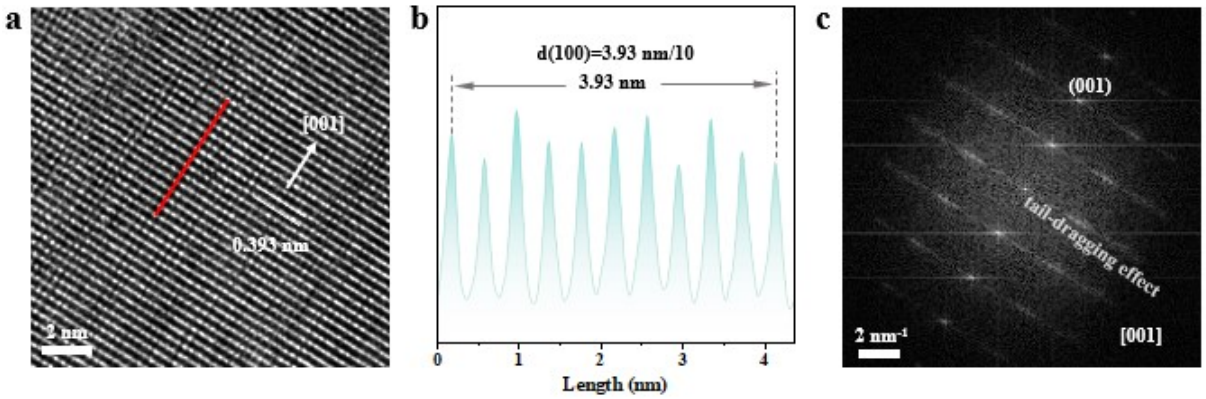

Fig. S10 Structural characterizations of other s-Ta_2O_5 NRs via TEM. (a) HRTEM image. (b) Lattice fringe interplanar spacings marked by the red line in Fig. S10a. (c) FFT pattern corresponding to Fig. S10a. Fig. S10a, b reveal that the average interplanar spacings of the (001) plane is 0.393 nm, slightly larger than that in typical Ta_2O_5 crystal, indicating a tensile strain along the [001] direction in s-Ta_2O_5 NRs. The associated FFT pattern of s-Ta_2O_5 NRs exhibits a tail-dragging effect, suggesting numerous disordered structures in the direction perpendicular to [001].

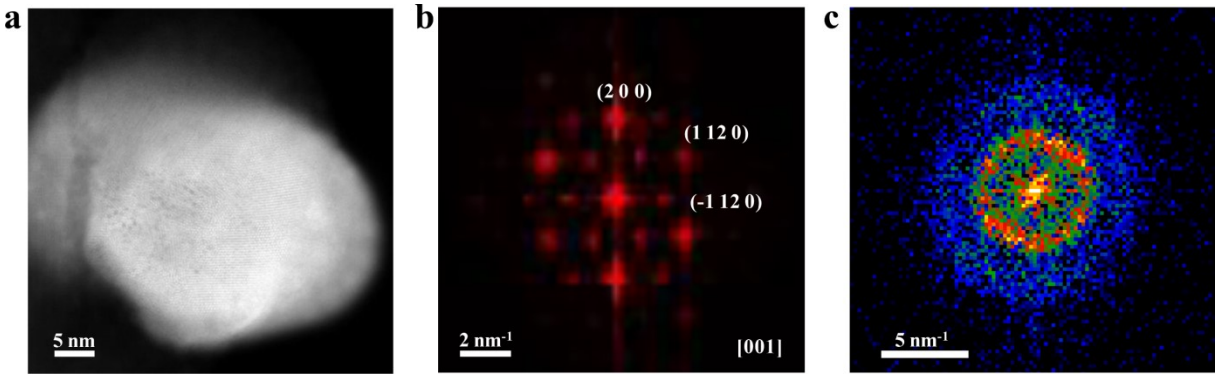

Fig. S11 Aberration-corrected TEM characterizations of cross-sections for the single s-Ta_2O_5 nanorod. (a) HAADF-STEM image. (b, c) Corresponding FFT patterns from Fig. 2g, i, respectively. A set of bright diffraction spots in Fig. S11b highlights the highly ordered atomic arrangements in this region. Conversely, a diffraction ring in Fig. S11c indicates a markedly disordered atomic arrangement.

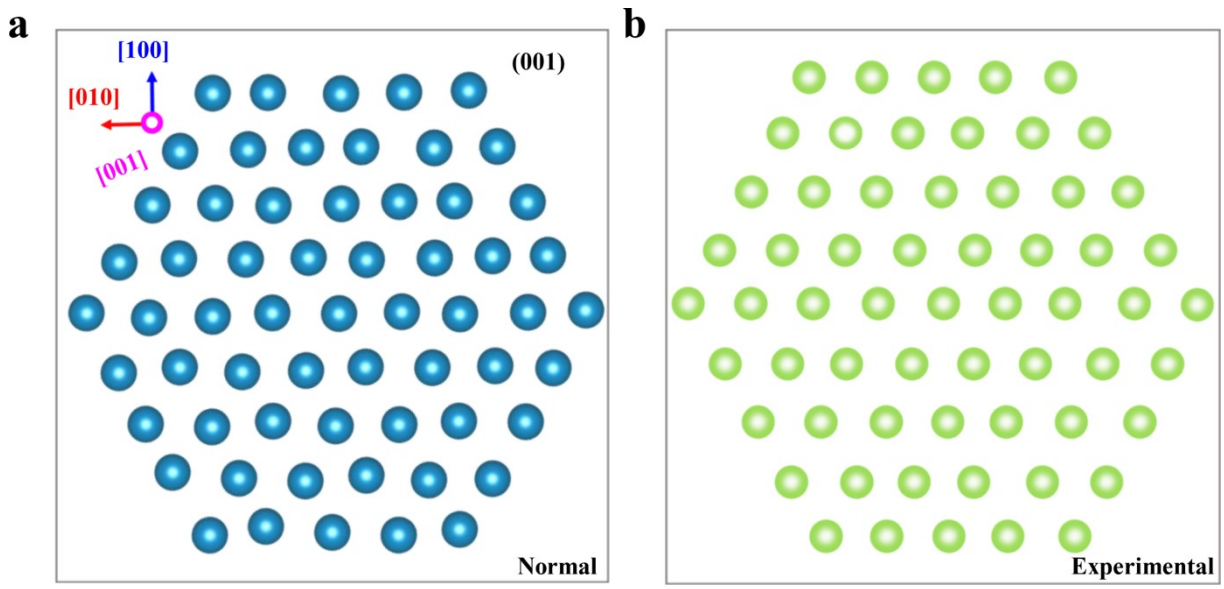

Fig. S12 Simulated atomic configurations of (001) planes. (a) Normal orthorhombic Ta_2O_5. (b) Ordered regions in s-Ta_2O_5 NRs. A comparison of Fig. S12a between 12b reveals that the atomic arrangement in the ordered sections of the s-Ta_2O_5 nanorods closely resembles that of the standard orthorhombic Ta_2O_5 phase, except for a minor increase in atomic spacing within the s-Ta_2O_5 NRs.

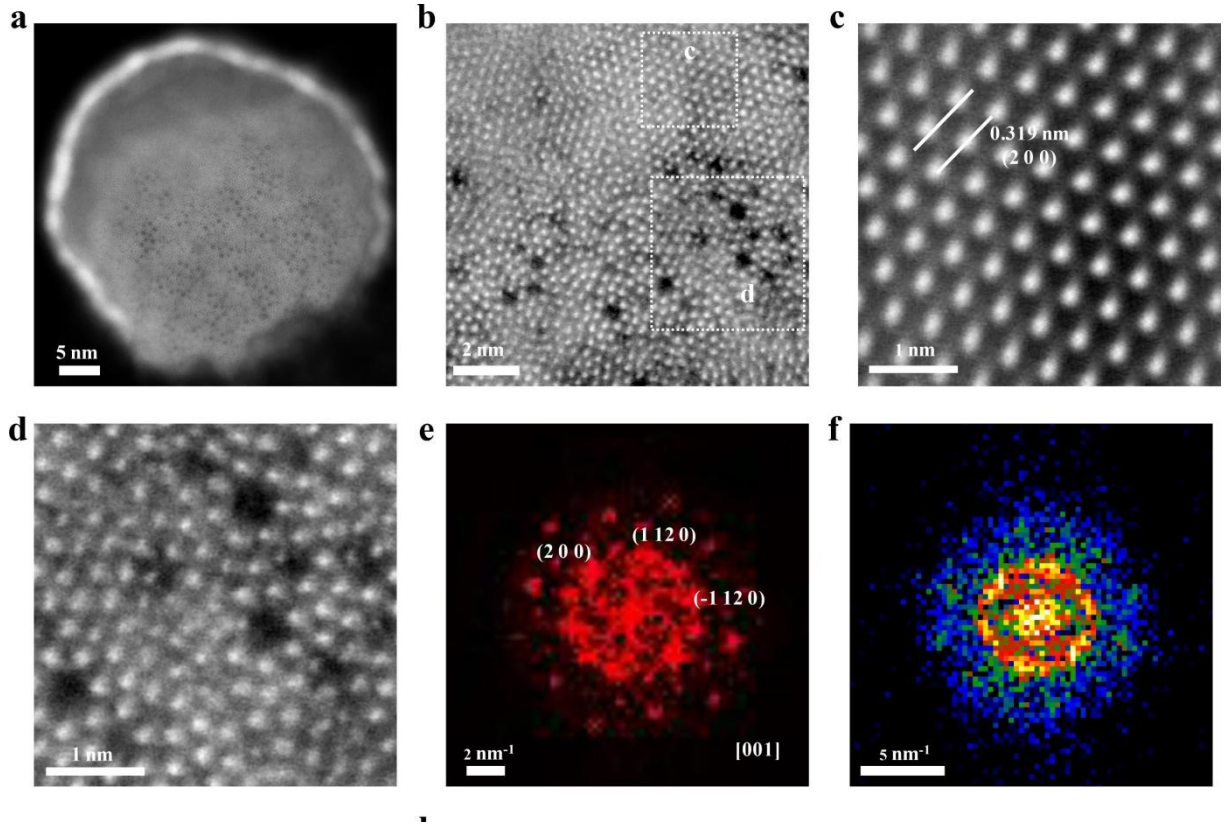

Fig. S13 Structural characterizations of cross-sections in other s-Ta_2O_5 NRs via aberration-corrected TEM. (a) HAADF-STEM image. (b) High-resolution HAADF-STEM image. (c, d) Enlarged HAADF-STEM images corresponding to the c and d rectangular square box areas in Fig. S13b, respectively. (e, f) Corresponding FFT patterns of Fig. S13c, d, respectively. The ordered and disordered atomic arrangements, along with a multitude of discernible cavities, can also be clearly observed in Fig. S13b. Fig. S13c shows a highly ordered arrangement of atoms similar to that in the orthorhombic Ta_2O_5 crystal, but exhibits a slightly larger interplanar spacing of 0.319 nm in the (200) plane (d(200)=0.31 nm, PDF# 25–0922). A set of bright diffraction spots in the corresponding FFT pattern supports the above results. In contrast, Fig. S13d displays a markedly disordered atomic arrangement, replete with numerous cavities, indicative of an amorphous structure. Only diffraction rings are observed in its corresponding FFT pattern.

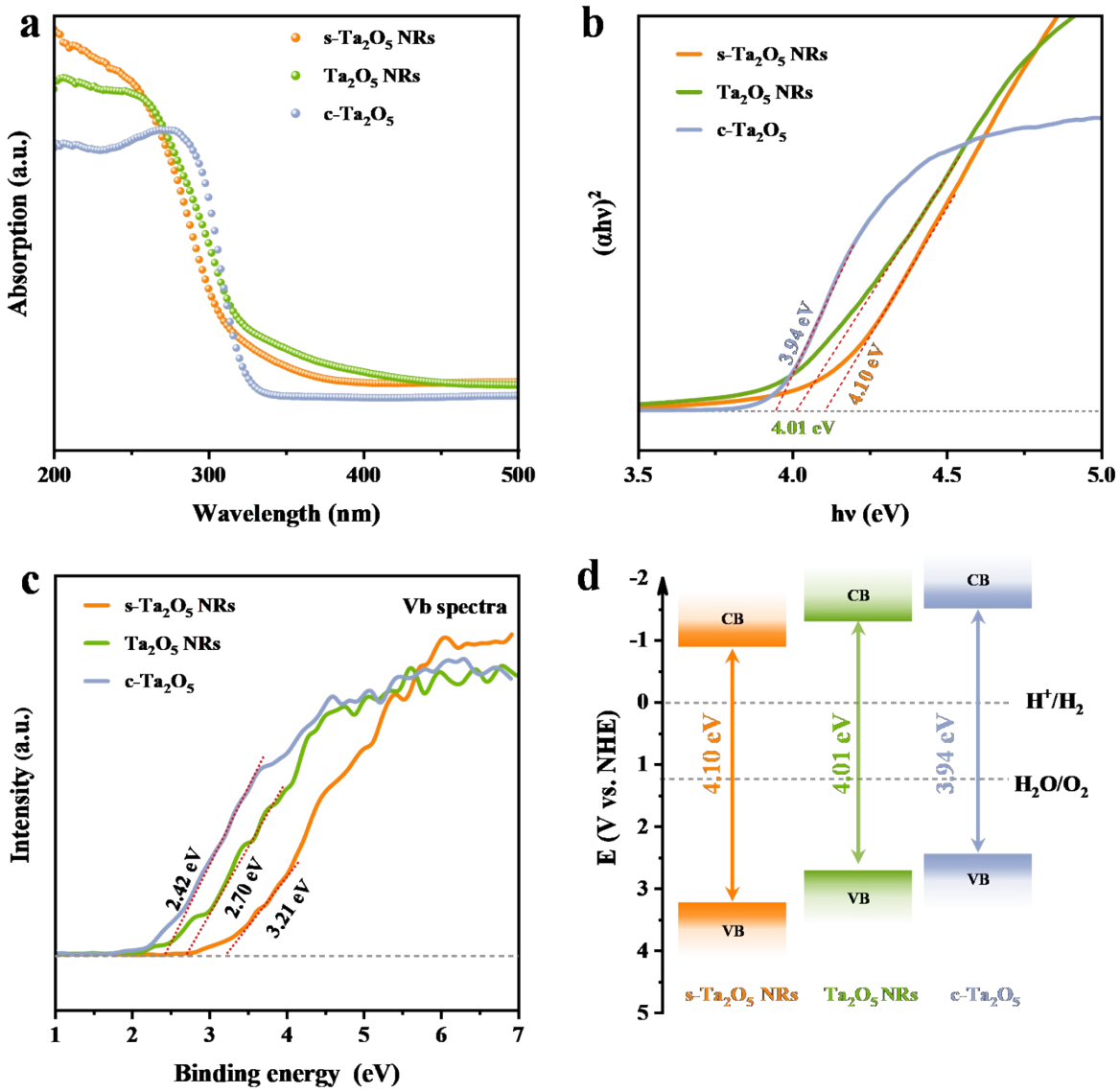

Fig. S14 Band structures of various Ta_2O_5 samples. (a) UV-vis absorption spectra. (b) Plots of $(\alpha h\nu)^2$ versus photon energy. (c) Valence-band spectra. (d) Band structure diagrams. It is evident that s-Ta_2O_5 NRs exhibit typical semiconductor properties, with a band structure akin to that of Ta_2O_5 NRs and c-Ta_2O_5, albeit with minor shifts in the valence and conduction band edges.

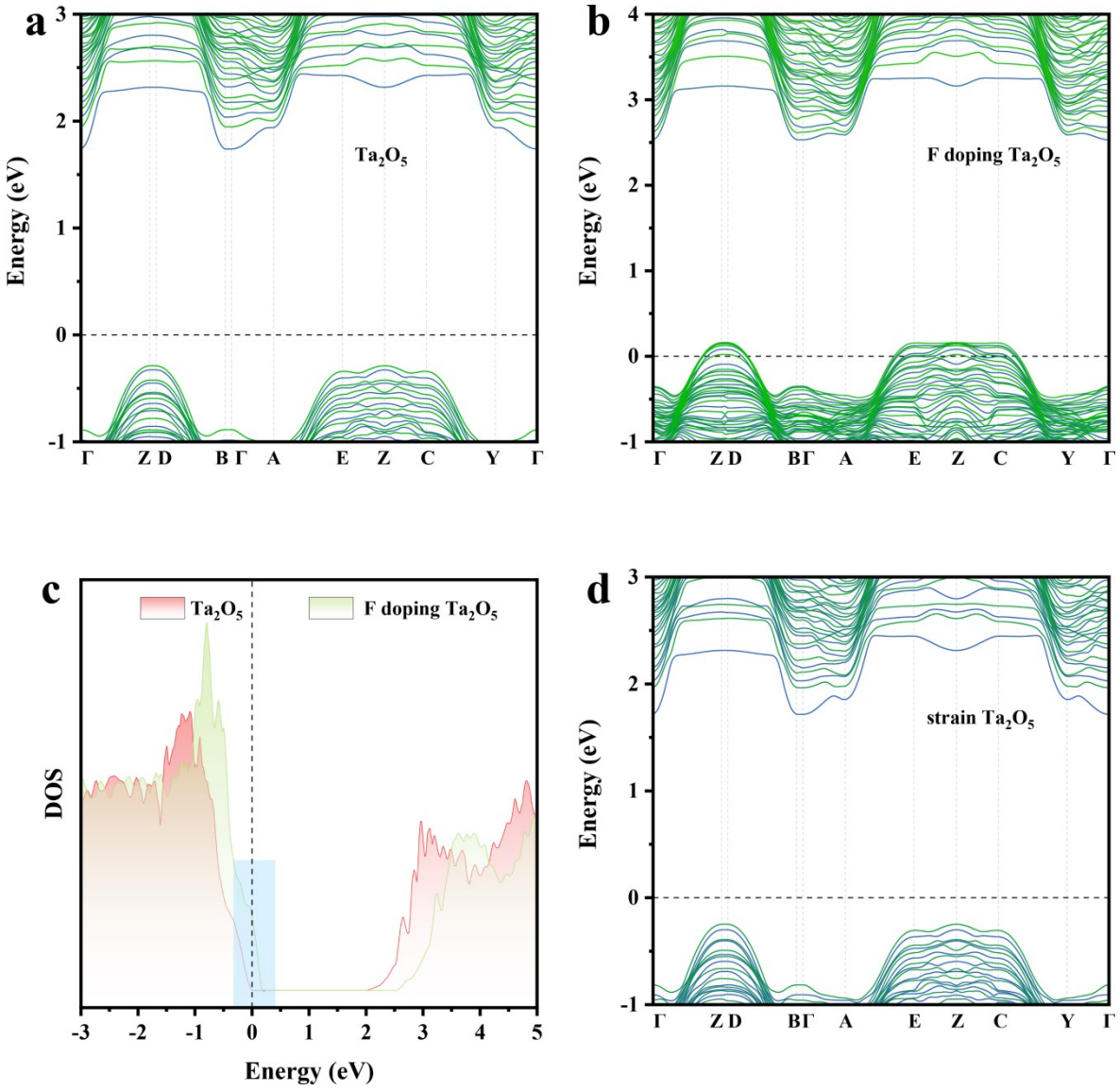

Fig. S15 Calculated band structures and DOS for various Ta_2O_5 models. (a) Band structure of the orthorhombic Ta_2O_5. (b) Band structure of the F-doped Ta_2O_5 crystal model. (c) DOS comparison between the conventional and F-doped Ta_2O_5 crystal models. (d) Band structure of Ta_2O_5 with tensile strain along the [001] direction.

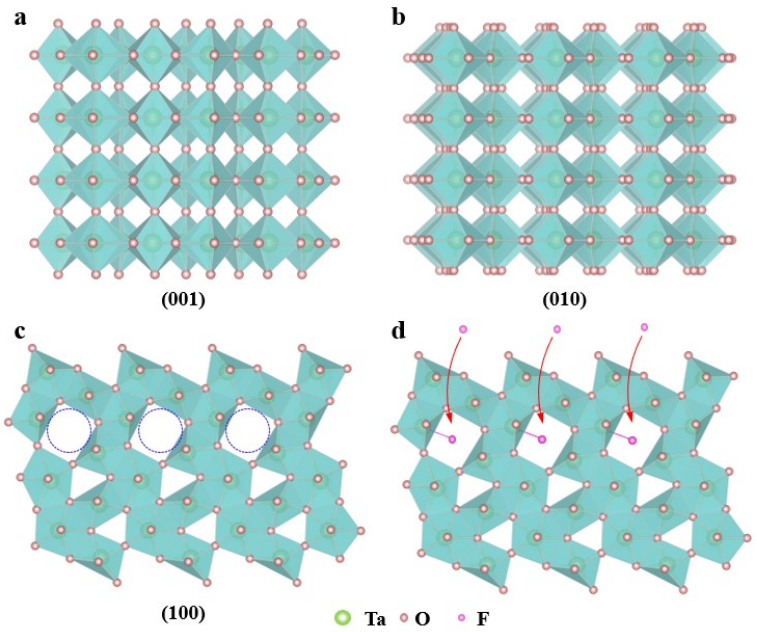

Fig. S16 The structural model of orthorhombic Ta_2O_5 and the potential insertion location for F.

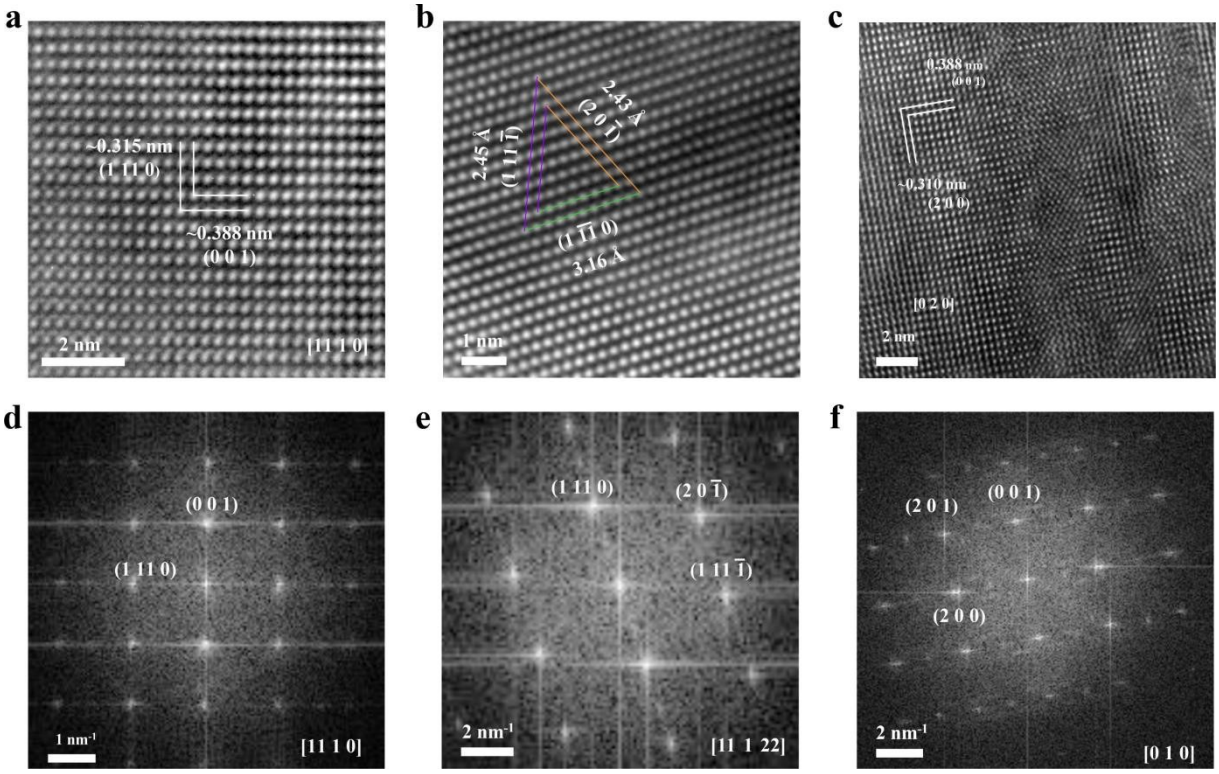

Fig. S17 Structural characterization of Ta_2O_5 NRs. HRTEM images taken with the electron beam along different directions. (a) [11 1 0], (b) [11 1 22], (c) [0 1 0]. (d, e, f) The FFT patterns corresponding to Fig. S17a-c respectively. In Fig. S17a, two sets of perpendicular lattice fringes are observed with spacings of ~0.388 nm and ~0.315 nm, corresponding to the (0 0 1) and (1 -11 0) planes of orthorhombic Ta_2O_5, respectively. In Fig. S17b, three sets of well-ordered lattice fringes with spacings of ~0.315 nm, ~0.245 nm, and ~0.243 nm were observed, corresponding to the (1 -11 0), (1 11 -1), and (2 0 -1) planes of orthorhombic Ta_2O_5, with interplanar angles of 71.8°, 43.3°, and 64.9°, respectively, which are consistent with the those of normal Ta_2O_5. Fig. S17c shows two sets of perpendicular lattice fringes with spacings of ~0.388 nm and ~0.31 nm, corresponding to the (0 0 1) and (2 0 0) planes of orthorhombic Ta_2O_5. Overall, HRTEM images collected from different directions all displayed well-ordered lattice fringes, fully consistent with the arrangement of a normal Ta_2O_5 crystal, indicating an orderly atomic arrangement within the Ta_2O_5 NRs. Moreover, the corresponding FFT patterns all exhibited bright diffraction spots, further confirming their well-crystallized monocrystalline structure. The above results, combined with the XRD, Raman, XAFS, and XPS analyses (Fig. 1c-h, and Fig. S3, S4, S8), consistently indicate that the amorphous F-doped Ta_2O_5 regions transform into ordered crystalline Ta_2O_5 after the 750°C annealing treatment to remove

F, leading to the disappearance of the tensile strain in s-Ta_2O_5, further suggesting that the local amorphization regions in s-Ta_2O_5 NRs are the key factor for inducing tensile strain.

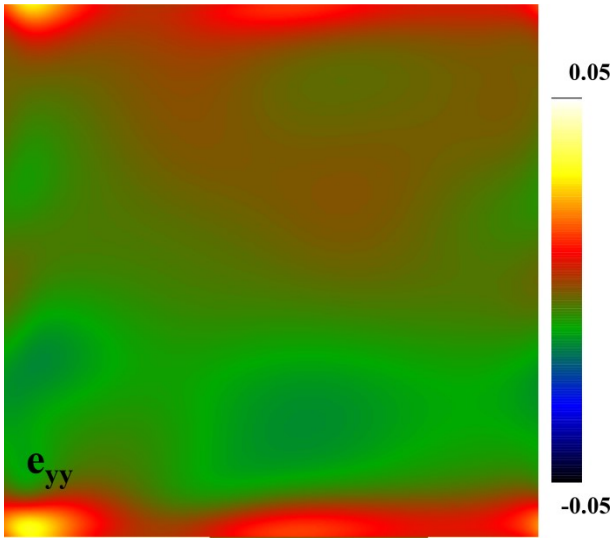

Fig. S18 The corresponding e_{yy} strain tensor mapping by GPA of Fig. S17a. It showed no strain within Ta_2O_5 NR, aligning with the XRD and Raman analysis results (Fig. 1c, d).

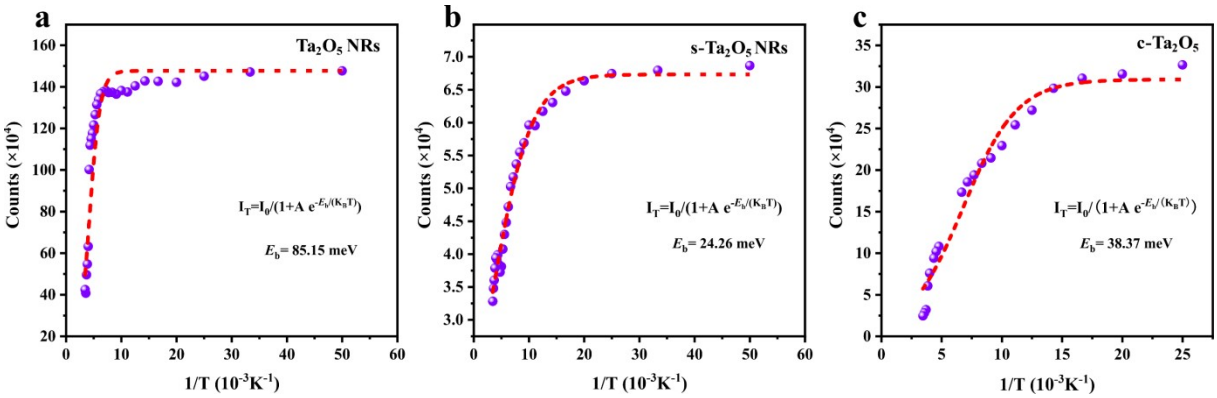

Fig. S19 Integrated PL emission intensity versus temperature for (a) Ta_2O_5 NRs. (b) s-Ta_2O_5 NRs. (c) c-Ta_2O_5.The E_b of Ta_2O_5 NRs, s-Ta_2O_5 NRs and c-Ta_2O_5 is calculated to be 85.15, 24.26, 38.37 meV, by employing the Arrhenius equation $I_T=I_0/(1+ Aexp(-E_b/k_BT))$ to fit the acquired temperature-dependent PL data.

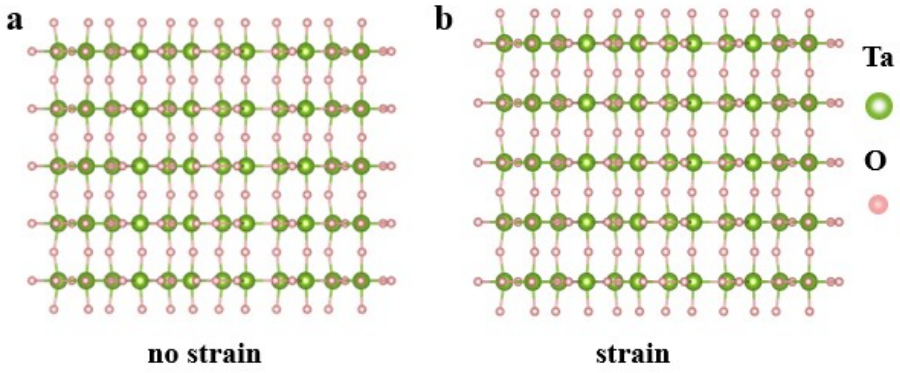

Fig. S20 The structural model of orthorhombic Ta_2O_5 (a)without and (b) with tensile strain.

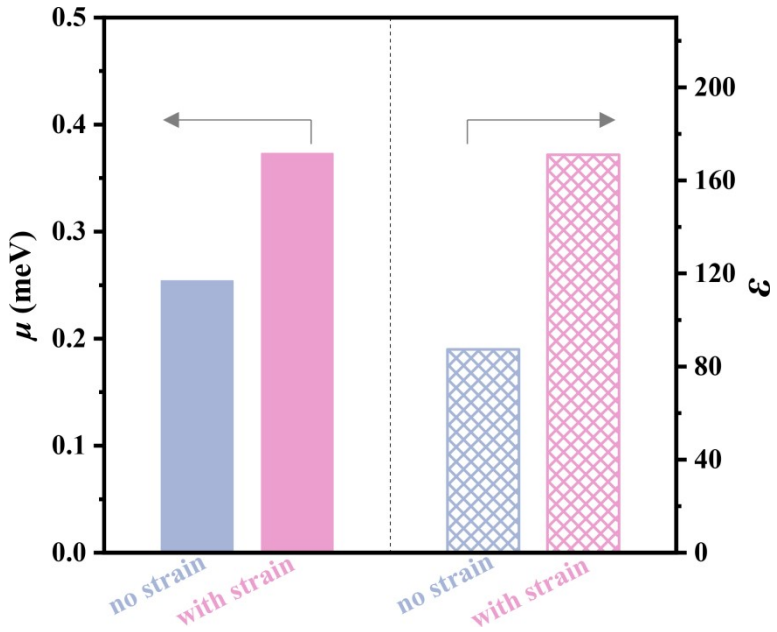

Fig. S21 Calculated μ and ε^2 values for Ta_2O_5 crystals along the [001] direction, with and without a tensile strain applied in this direction. Fig. S21 illustrates that a tensile strain along the [001] direction marginally increases μ, while ε_r^2 experiences a considerable increase, resulting in an enhanced dielectric screening effect. Consequently, the introduction of a tensile strain along the [001] direction is calculated to cause a 61.67% decrease in E_b, aligning well with the experimentally observed trends in E_b variation.

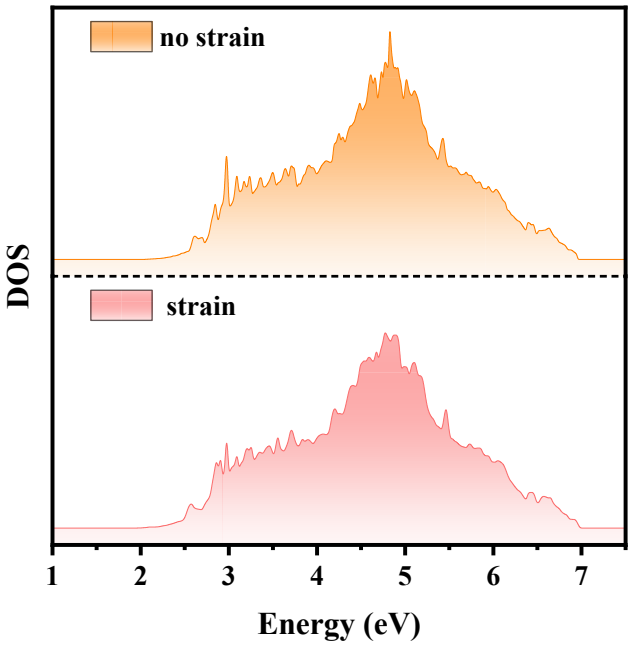

Fig. S22 O 2*p* PDOS for Ta_2O_5 models with/without tensile strain along the [001] direction. As shown in Fig. S22, after applying a tensile strain, Ta_2O_5 models, irrespective of the presence or absence of tensile strain along the [001] direction, demonstrate comparable O 2*p* PDOS behavior above the Fermi surface, albeit with a slight reduction in intensity.

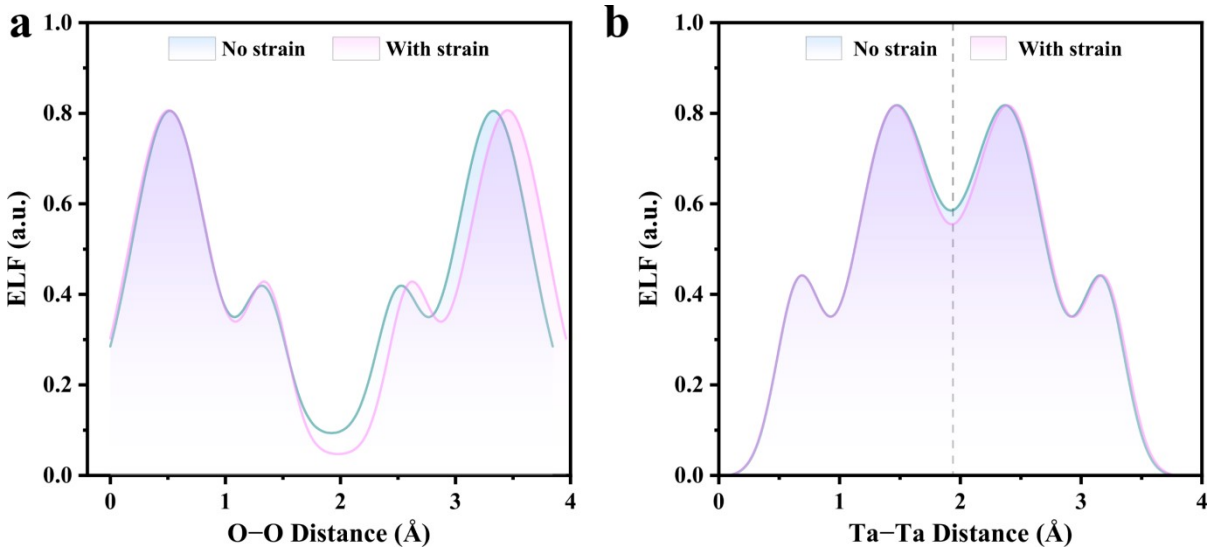

Fig. S23 ELF line profiles. (a) O−O and (b) Ta−Ta interatomic pairs in Ta_2O_5, with and without a tensile strain along the [001] direction.

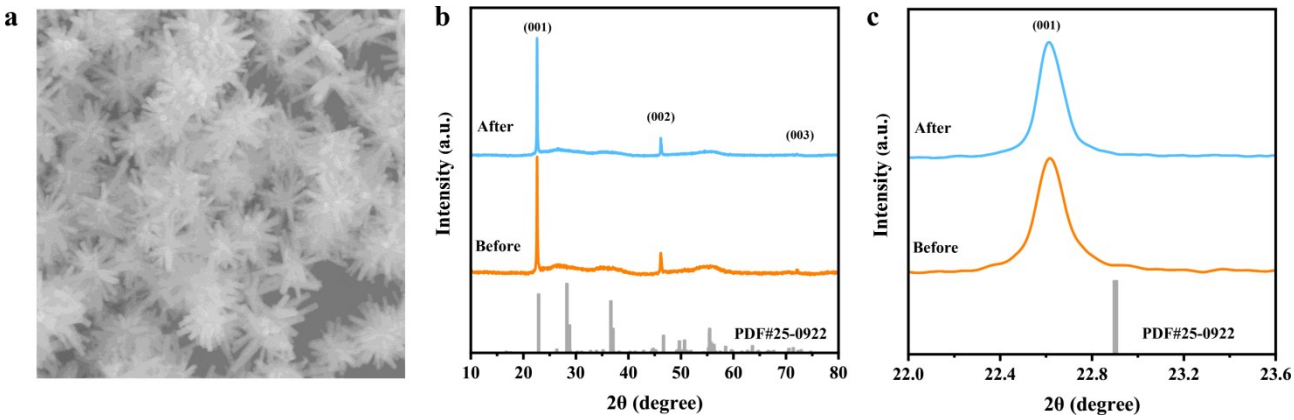

Fig. S24 Structural characterizations of s-Ta_2O_5 NRs before and after photocatalysis. (a) SEM image after photocatalysis. (b) XRD patterns. (c) Enlarged view of the (001) peaks. Fig. S24 shows that the morphology and phase of s-Ta_2O_5 NRs were mostly unaltered following the photocatalytic reaction, indicating their high stability.

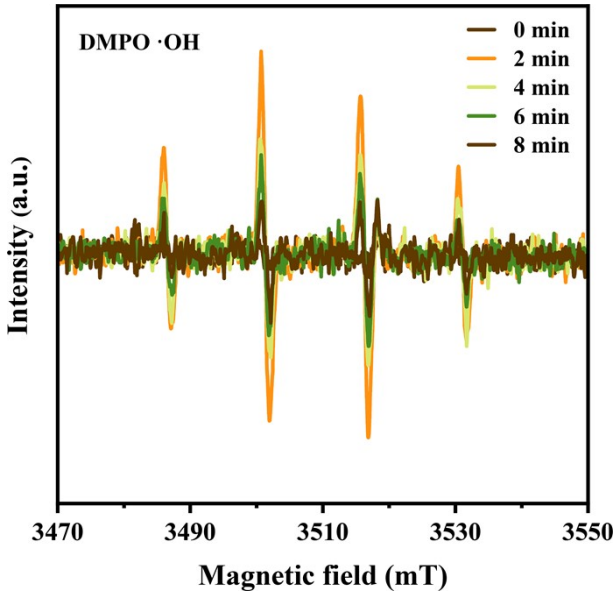

Fig. S25 In-situ ESR spectra of DMPO-trapped ·OH radicals in s-Ta_2O_5 NRs under photoillumination.

Table S1 EXAFS curves fitting results

Sample	Shell	N	R (Å)	$\Delta\sigma^2*10^3$ ($Å^2$)	$\triangle E_0$ (eV)	R-factor
Ta [a]	Ta-Ta1	8.0	2.86	5.08	3.7	0.8
	Ta-Ta2	6.0	3.30	6.86	5.7	
Ta_2O_5 NRs [b]	Ta-O1	4.0	1.89	11.61	-5.1	0.3
	Ta-O2	2.0	2.04	4.35	8.6	
1-s-Ta_2O_5 [b]	Ta-F	0.5	1.81	2.75	-4.5	0.6
	Ta-O	5.6	1.95	11.92	2.0	
2-s-Ta_2O_5 [b]	Ta-F	0.4	1.81	11.94	-7.3	0.6
	Ta-O1	1.4	1.90	6.32	1.8	
	Ta-O2	4.0	2.05	2.78	1.8	

N, coordination number; R, distance between absorber and backscatter atoms; σ^2, Debye-Waller factor to account for both thermal and structural disorders; ΔE_0, inner potential correction; R-factor (%) indicate the goodness of the fit.

The obtained S_0^2 of Ta and Pt foil were 0.95, and they were fixed in the subsequent fitting of Ta L3-edge for the catalyst, respectively.

[a]Ta L_3-edge EXAFS curves fitting parameters: $\Delta k = 3.0 – 12.0 Å^{-1}$, $\Delta r = 1.0 – 3.5$ Å.

[b]Ta L_3-edge EXAFS curves fitting parameters: $\Delta k = 3.0 – 12.0 Å^{-1}$, $\Delta r = 1.0 – 2.4$ Å.

Note S1 Raman spectra analyses

Raman spectra of Fig. 1d reveals seven prominent vibrational modes inherent to orthorhombic Ta_2O_5, with peaks at 65.5, 97.4, 195.3, 243.9, 615.4, 702.4, and 843.2 cm^{-1}. These peaks within the 100-450 cm^{-1} range are predominantly associated with the bending vibrations of the O-Ta-O bonds within the TaO_6 octahedra, while those in the 450-900 cm^{-1} range are indicative of Ta-O stretching vibrations related to edge-sharing polyhedra distortions.[8-11] Specifically, the peaks at 243.9, 615.4, 702.4, and 843.2 cm^{-1} are respectively ascribed to the bending vibration of bridging Ta-O-Ta, the symmetric stretching vibration of Ta-O, the asymmetric stretching vibration of bridging Ta-O-Ta, and the higher-order symmetric stretching vibration of Ta-O, respectively. A slight redshift in the Raman signal of s-Ta_2O_5 NRs, specifically in the O-Ta-O and Ta-O stretching vibrations, corroborates the introduction of tensile strain within the lattice. Additionally, an increase in the relative intensity ratio of certain vibrational modes in s-Ta_2O_5 suggests a rise in edge-sharing Ta-O bonds and a concurrent emergence of amorphous regions. The reduced vibrational intensity further points to a reduction in crystallinity for s-Ta_2O_5.

References

1 Kresse and Hafner, *Phys. Rev. B*, 1993, **47**, 558-561.

2 V. Wang, N. Xu, J.-C. Liu, G. Tang and W.-T. Geng, *Comput. Phys. Commun.*, 2021, **267**, 108033.

3 J. H. Choi, P. Cui, H. P. Lan and Z. Y. Zhang, *Phys. Rev. Lett.*, 2015, **115**, 066403.

4 B. Silvi and A. Savin, *Nature*, 1994, **371**, 683-686.

5 E. L. Lee and I. E. Wachs, *J. Phys. Chem. C*, 2007, **111**, 14410-14425.

6 M. Baranowski and P. Plochocka, *Adv. Energy Mater.*, 2020, **10**, 1903659.

7 M. Bokdam, T. Sander, A. Stroppa, S. Picozzi, D. D. Sarma, C. Franchini and G. Kresse, *Sci. Rep.*, 2016, **6**, 28618.

8 V. Janakiraman, V. Tamilnayagam, R. S. Sundararajan, S. Suresh and C. S. Biju, *J. Mater. Sci. Mater. Electron.*, 2021, **32**, 9244-9252.

9 H. Benchorfi, S. Chenu, J.-R. Duclere, C. Genevois, M. Allix, E. Veron, J. Cornette, M. Colas, V. A. G. Rivera, V. Fuertes, F. Brisset, P. Carles, S. Aouji, P. Thomas, Y. Messaddeq and G. Delaizir, *J. Eur. Ceram. Soc.*, 2024, **44**, 1131-1142.

10 Z. Zhang, Z. Li, L. Wang, J. Li, J. Pan, S. Wang, C. Zhang, Z. Li, Q. Peng and X. Xiu, *Opt. Express*, 2021, **29**, 34552-34564.

11 P. S. Dobal, R. S. Katiyar, Y. Jiang, R. Guo and A. S. Bhalla, *J. Raman Spectrosc.*, 2000, **31**, 1061-1065.